Journal of Electron Spectroscopy and Related Phenomena 224 (2018) 45–50

Contents lists available at ScienceDirect

Journal of Electron Spectroscopy and Related Phenomena

journal homepage: www.elsevier.com/locate/elspec

Capabilities of Angle Resolved Time of Flight electron spectroscopy with the 60° wide angle acceptance lens

Danilo Kühn[a,*,1], Florian Sorgenfrei[a,1], Erika Giangrisostomi[b], Raphael Jay[a], Abdurrahman Musazay[b], Ruslan Ovsyannikov[b], Christian Stråhlman[b,2], Svante Svensson[c], Nils Mårtensson[c], Alexander Föhlisch[a,b]

[a] Institut für Physik und Astronomie, Universität Potsdam, Karl-Liebknecht-Str. 24/25, D-14476 Potsdam, Germany
[b] Helmholtz-Zentrum Berlin für Materialien und Energie GmbH, Albert-Einstein-Straße 15, 12489 Berlin, Germany
[c] Department of Physics and Astronomy, Box 516, 75120 Uppsala, Sweden

ARTICLE INFO

Article history:
Received 19 December 2016
Accepted 27 June 2017
Available online 11 July 2017

Keywords:
Artof
Electron spectroscopy
Wide angle
Time of flight
Energy resolution
Synchrotron

ABSTRACT

The simultaneous detection of energy, momentum and temporal information in electron spectroscopy is the key aspect to enhance the detection efficiency in order to broaden the range of scientific applications. Employing a novel 60° wide angle acceptance lens system, based on an additional accelerating electron optical element, leads to a significant enhancement in transmission over the previously employed 30° electron lenses. Due to the performance gain, optimized capabilities for time resolved electron spectroscopy and other high transmission applications with pulsed ionizing radiation have been obtained. The energy resolution and transmission have been determined experimentally utilizing BESSY II as a photon source. Four different and complementary lens modes have been characterized.

1. Introduction

Electron spectroscopy has been a powerful experimental technique for investigating matter in all phases since its development in the 1960s by Kai Siegbahn. Advancing simultaneous detection of both electron kinetic energies and their angular or momentum distribution has been the pathway to enhance the experimental performance. In this respect, the combination of an advanced electron optical lens with an hemispherical deflection analyzer (HDA) [1] established a workhorse that links high energy resolution, high angular resolution and flexibility in operation modi spanning from highest transmission and energy resolution to combined high angular and energy resolving operation. In order to avoid the geometric constraints of the HDA entrance slit, the energy dispersive hemisphere can be replaced by a high transmission Time of Flight energy dispersing unit. This has led to the development of the Angle Resolved Time of Flight Analyzer (ARTOF) [2]. Operating at an acceptance angle of 30° the approach was established in proof of principle experiments, utilizing the single bunch time structure of synchrotron radiation and laboratory sources [3–6]. Since the electron flight time within the ARTOF sets an upper limit for the suitable repetition rate for the photon source in the range of few MHz, a reduction of the GHz repetition rates of multibunch synchrotron radiation, i.e. 500 MHz at BESSY II, is crucial for a wider application of this advanced electron spectrometer. Thus BESSY II has developed Pulse Picking by Resonant Excitation (PPRE) [7] and mechanical pulse selection by a MHz Chopper [8] as well as electronic detector gating [9].

Combining these advances, we have now taken the step to enhance the acceptance angle of the ARTOF lens system through an additional accelerating electron optical element which allows to widen the angular acceptance to 60° keeping both energy and angular resolution. Utilizing the BESSY II FEMTOSPEX installations [10] in this work we present the working principle and the experimental parameter space of the 60° ARTOF system.

2. Electron analyzer and setup

The 60° wide angle acceptance ARTOF is the core of the new end station for surface and solid state dynamics at the BESSY II soft X-Ray femto slicing beamline.

* Corresponding author.
E-mail address: danilo.kuehn@helmholtz-berlin.de (D. Kühn).
[1] Previous address: Helmholtz-Zentrum Berlin für Materialien und Energie GmbH, Albert-Einstein-Straße 15, 12489 Berlin, Germany.
[2] Present address: Malmö University, 20506 Malmö, Sweden.

https://doi.org/10.1016/j.elspec.2017.06.008

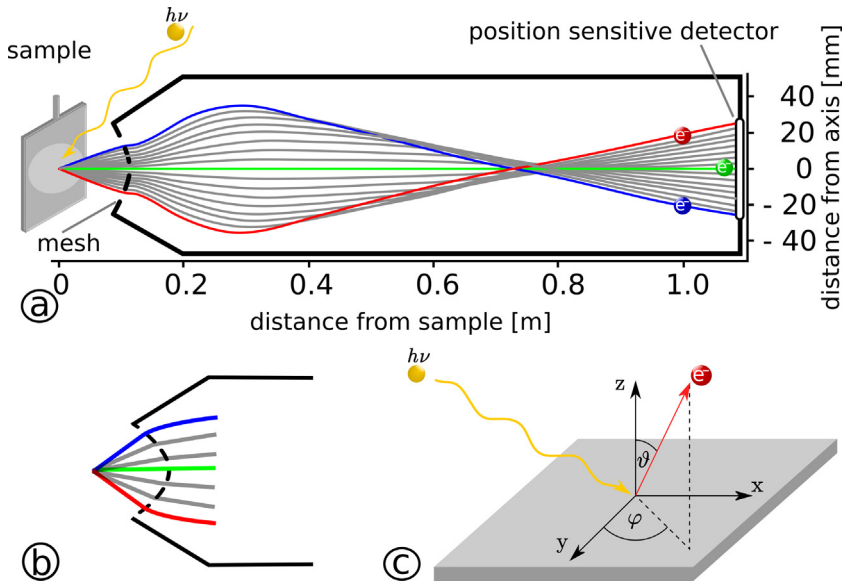

Fig. 1. a) Schematic drawing of the 60° wide angle acceptance ARTOF. Electrons emitted from the sample under high angles with respect to the surface normal (red and blue lines), are deflected strongly towards the optical axis (green line) when entering the spectrometer entrance due to the retardation mesh. Depicted electrons close to the detector mark equal flight times. b) Insight of the ARTOF entrance c) Photoemission geometry.

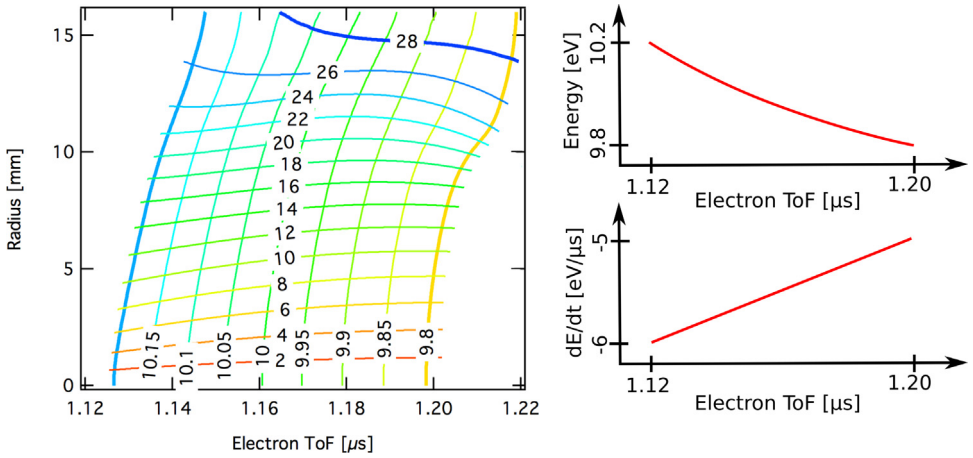

Fig. 2. Left: Contour plot of the simulated conversion matrices for the Ang56_4-lens mode for E_{cen} = 10eV. The vertical lines mark equivalent energies in eV and the horizontal lines mark equivalent angle ϑ in deg. Right: Schematic energy vs. time-of-flight dependency for $\vartheta = 0$ (top) and its derivative $\frac{\partial E}{\partial t}$ (bottom).

The ARTOF is a Time of Flight electron spectrometer which consists of a 1.3 m long drift tube with an advanced electrostatic lens system of multiple lens elements and a two-dimensional delay line detector by Roentdek GmbH including a MCP electron multiplier which enables event detection of arrival time and position of every analyzed electron. The wide angle lens is a modular upgrade of the ARTOF lens system with an electron retardation mesh at the ARTOF entrance with 80% transmission providing a deflection of all electron trajectories within the high acceptance angle into the drift tube. Fig. 1 shows a schematic drawing of the ARTOF with trajectories of electrons emitted under different angles ϑ, φ after optical excitation of the sample. Electrons emitted under higher angles ϑ with respect to the optical axis of the spectrometer have longer flight paths and thus longer flight times compared to electrons emitted on axis ($\vartheta = 0$). The electron arrival time t and hitting position x,y at the detector depend on the kinetic electron energy E and the take-off angle ϑ in a non-linear way and can be transformed to energy E and emission angles ϑ, φ by two transformation matrices in cylindrical coordinates $E(t, r)$ and $\vartheta(t, r)$ which are obtained by simulations [2] (see Fig. 2). The φ-matrix is trivial due to cylindrical symmetry.

The ARTOF is operated in the constant retardation ratio (CRR) mode which means that all voltages of the lens system are raised proportionally to the center energy E_{cen} of the analyzed energy window. Conclusively the electron trajectories are independent from E_{cen} and only one set of conversion matrices is necessary to cover the transformation for the full energy range. The energy window is a constant fraction of E_{cen} and the energy resolution is scaling with $E^{3/2}$ according to Eq. (1) for high energies. In this operation mode one can define a lens mode by specifying all lens element voltages for a single energy e.g. E_{cen} = 10eV. The size of the energy window in which all electrons can be analyzed simultaneously and the angle acceptance can be derived from simulations. The standard nomenclature of a lens mode is 'Angθ_ew' where θ is the full angle acceptance and 'ew' is the size of the energy window in percentage e.g. 'Ang56_4'.

All measurements in this work have been performed at the UE 56/1 PGM soft X-Ray beamline at the BESSY II in standard multibunch mode. While commonly operating with PPRE [7] we here used the unexcited Camshaft bunch in the middle of the ion clearing gap to avoid any possible decrease in beamline energy resolution which might arise from bunch excitation. We have chosen the

1200 l/mm monochromator grating and the 50 μm exit slit for optimal beamline energy resolution and small electron spot size at the sample respectively. The photon beam is vertically polarized and the photon energy ranges between 260 and 970 eV with a photon pulse length <70 ps FWHM. The ARTOF optical axis is parallel to the sample surface normal and lies in the beam plane. The photon beam is hitting the sample under 50° with respect to the surface normal. The base pressure of the experimental chamber is $2{\cdot}10^{-10}$ mbar and all measurements were performed at room temperature.

3. Results

One of the most important characteristics of an electron spectrometer is its energy resolution ΔE and the related resolving power E/ΔE. We have analyzed this property in the soft X-Ray regime for kinetic electron energies between 90 eV and 810 eV. In the CRR mode the energy resolution is given by the following equation:

$$\Delta E = \sqrt{\left(\alpha \cdot E^{3/2} \cdot \Delta t\right)^2 + \left(\beta \cdot E \cdot \Delta d\right)^2} \quad (1)$$

The first part of this equation contains the contribution from the temporal resolution Δt, the second part describes the effect of the spatial detector resolution Δd. The parameters α and β describe the temporal energy dispersion and spatial energy dispersion, respectively, and depend on the specific lens mode. They are generally a function of detector hit position and flight time (examples are given below). Further contributions may come from the electron source diameter and a rotated sample surface that is not perpendicular to the optical axis of the spectrometer. However for high kinetic energies E_{kin} > 50 eV and small spot sizes ≈100 μm as typically exist at a synchrotron radiation beamline, the temporal resolution is the dominating contribution to the intrinsic energy resolution [2] and Eq. (1) simplifies to Eq. (2):

$$\Delta E = \alpha \cdot E^{3/2} \cdot \Delta t \quad (2)$$

The total temporal resolution Δt is given by the convolution of the exciting photon pulse length Δt_{ph} = 70ps FWHM and the temporal resolution of the detector Δt_{det}

$$\Delta t = \sqrt{\Delta t_{ph}^2 + \Delta t_{det}^2} \quad (3)$$

and can be determined by measuring only photons at the detector, which is achieved by applying a large negative bias. Here we determine $\Delta t = 216 \pm 2$ps FWHM for the global temporal resolution by applying a Gaussian fit to the photon signal integrated over the whole detector area and $\Delta t = 166 \pm 13$ps FWHM for the detector position adapted temporal resolution, as provided by the photon peak fit tool available within the ARTOF LOADER analysis package.[3]

For the analysis of the energy resolution we distinguish between local energy resolution ΔE_{loc} where the electron spectra are determined only from a small detector area around the origin and the global energy resolution ΔE_{glob} where the whole angle acceptance is used to derive the spectra. Besides the fundamental limit of the energy resolution given by the temporal resolution, the global energy resolution can be further affected by residual misalignments and signal propagation time differences of the detector whereas the local energy resolution is only little affected by those. Therefore deviations between ΔE_{loc} and ΔE_{glob} for a given setting can give hints of 'how far the spectrometer is away from optimal performance'.

In this work we use the S2p photoemission lines of semiconducting 2H-MoS_2 for the characterization of the energy resolution. The sample is prepared by cleaving, which gives reliably clean surfaces leading to a well defined electron source geometry. The $S2p_{3/2}$ and $S2p_{1/2}$ peaks with E_{bind} =162.7 eV and E_{bind} =163.9 eV [11] respectively have a narrow symmetric line shape with a natural line width of 0.054eV[4] and give a good signal to background ratio. We observe an additional constant Gaussian line broadening of ΔE_{sample} = 0.19 eV FWHM which is dominating the line width at kinetic energies below 100 eV. This was also observed by Mattila et al. and is attributed to terraces, steps and point defects at the sample surface [11]. In Fig. 3 different representations of the spectra for two different kinetic energies are shown for the Ang56_4-lens mode. The energy-angle-cuts (top and middle panels) show the intensity of the S2p lines over the whole angle acceptance revealing only minor distortions. The energy spectra which are integrated over a small detector area and the whole detector area respectively, have very similar line shapes and show only a minor additional broadening in the latter case. The count rates of the different lens modes give qualitative proof of the increased transmission for the 60° instrument. The intensity ratio of the S2p lines of Ang60 and Ang50 lens modes is about 1.4, in accordance with the ratio of the solid angles. However, the quantitative differences between Ang56, Ang58 and Ang60 are difficult to determine precisely due to the inhomogeneous angular distribution of the emitted electrons.

For quantifying the energy resolution we have measured S2p photoelectron spectra for five different kinetic energies in four different lens modes and applied a fit consisting of two Voigt profile peaks with a fixed spin orbit splitting of 1.19 eV, a Lorentzian width of 0.054 eV convolved with a Gaussian broadening and a linear background (see e.g. Fig. 4a). The center energy is set to the kinetic energy of the S2p lines for each measurement. The spectrometer energy resolution can now be calculated by deconvolving the Gaussian line width from the sample broadening and the beamline resolution ΔE_{ph}. In a next step we have determined the scaling parameter $\alpha{\cdot}\Delta t$ in Eq. (2) by applying a fit (Eq. (4)) to the global Gaussian line width (see Fig. 4b) and the local Gaussian line width, respectively (see Table 1).

$$\Delta E = \sqrt{\left(\alpha \cdot \Delta t \cdot E_{kin}^{3/2}\right)^2 - \left(\Delta E_{ph}\right)^2 - \left(\Delta E_{sample}\right)^2} \quad (4)$$

Using $\alpha_{loc}{\cdot}\Delta t$ and $\alpha_{glob}{\cdot}\Delta t$ one can calculate the local and global energy resolution (see Fig. 5a) and the resolving power (see Fig. 5b).

The parameters α and β from Eq. (1) can also be determined from the simulated energy conversion matrices $E(t, r)$ by numerical differentiation with respect to the time of flight (t) or position on the detector (radius r).

$$\alpha_{matr}(t, r) = -\frac{\partial E(t, r)}{\partial t} \cdot E_{cen}^{-3/2} \quad (5)$$

$$\beta_{matr}(t, r) = \frac{\partial E(t, r)}{\partial r} \cdot E_{cen}^{-1}$$

The parameters depend on r and t it is therefore not possible to give a single energy resolution for a given lens mode. For all lens modes one can observe a rather narrow distribution of alpha values around $\alpha_{matr}(r = 0, E = E_{cen})$(see Table 1). The relative width of the distribution $\Delta\alpha_{matr}/\alpha_{matr}$ is approximately ±15%. The value for β_{matr} is rather homogeneously distributed between β_{matr} = 0 for r = 0 and $\beta_{matr} = 1.5\ m^{-1}$ for higher radii. The contributions of spatial and temporal resolution on the energy resolution are about equal between E_{cen} =10 eV and 30 eV and the temporal resolution becomes increasingly dominant for $E_{cen} \geq 50$ eV.

[3] ARTOF LOADER v. 2.5.–156, see ref. [4] for further informations.

[4] M. Krause and J.H. Oliver J. Phys. Chem. Ref. Data, Vol 8, No. 2, 1979.

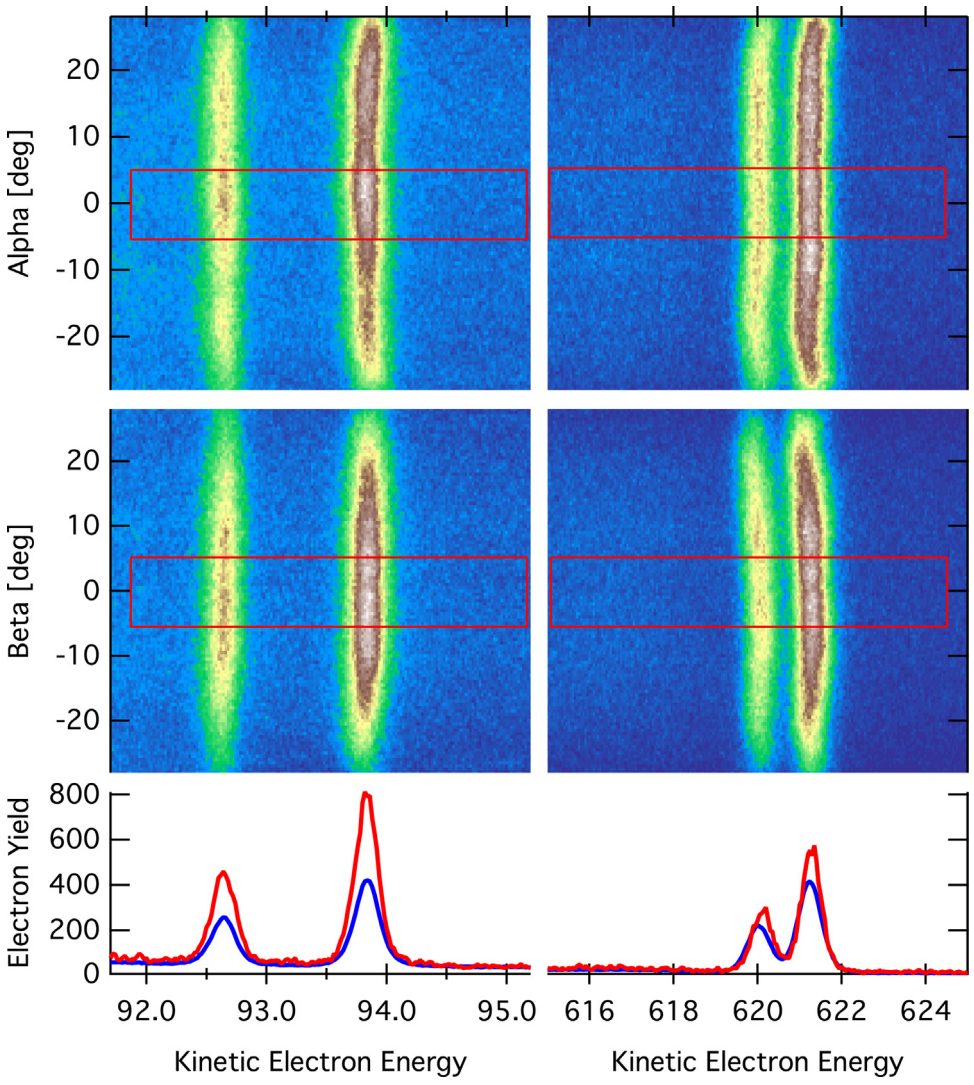

Fig. 3. Angle/energy 2D maps for two different kinetic energies (left: E_{ph} = 260 eV, right: E_{ph} = 790 eV) recorded in the Ang56_4-lens mode represented in bipolar coordinates. On the top panels, intensity is displayed vs. energy and the vertical angle alpha and integrated over the horizontal angle beta. In the middle panels, intensity is displayed vs. energy and beta and integrated over alpha. At the bottom panel, angle integrated energy spectra are plotted for two different integration areas: The red spectra are taken from an area around the detector origin (marked by red boxes in 2D plots) and the blue spectra are taken from full angle acceptance. The small area spectra show real electron yield (counts) while the full angle acceptance spectra are normalized to solid angle (scaling factor amounts to 30.8). Note that only a fraction of the recorded energy window is displayed for both kinetic energies.

Table 1
List of experimental and simulated lens mode parameters determining the energy resolution according to Eq. (2) and the angular resolution.

	Energy window [%]	$\alpha_{loc} \cdot \Delta t$ (local) $\left[10^{-5}\mathrm{eV}^{-0.5}\right]$	$\alpha_{glob} \cdot \Delta t$ (global) $\left[10^{-5}\mathrm{eV}^{-0.5}\right]$	$\frac{\alpha_{loc}}{\alpha_{glob}}$	α_{matr} $\left[10^{5}\mathrm{eV}^{-0.5}\mathrm{s}^{-1}\right]$	Angular resolution [deg]
ang50	7	5.34 ± 0.04	6.95 ± 0.02	0.77	3.43	0.13 ± 0.02
ang56	4	3.06 ± 0.03	3.67 ± 0.01	0.83	1.76	0.18 ± 0.04
ang58	4	3.41 ± 0.02	4.18 ± 0.01	0.82	1.93	0.20 ± 0.04
ang60	2	4.17 ± 0.03	4.88 ± 0.01	0.85	2.54	0.15 ± 0.02

The angular resolution can be estimated from the angular dispersion of the lens system in the image plane at the detector by calculating the derivative of the theta conversion matrix. For source sizes $d_{source} \leq 100\,\mu m$, with a spatial detector resolution of Δd_{det} = 100 μm and neglecting the minor influence of temporal resolution, the angular resolution is given by:

$$\Delta\vartheta(r) \approx \frac{\partial\vartheta}{\partial r}(r) \cdot \Delta d_{det} \tag{6}$$

Table 1 shows the angular resolution averaged over the acceptance angle for all lens modes. The uncertainties are given as standard deviations.

4. Discussion

The local energy resolution determined from the S2p peak fits can be directly compared with the expected energy resolution from the energy conversion matrices with the temporal resolution

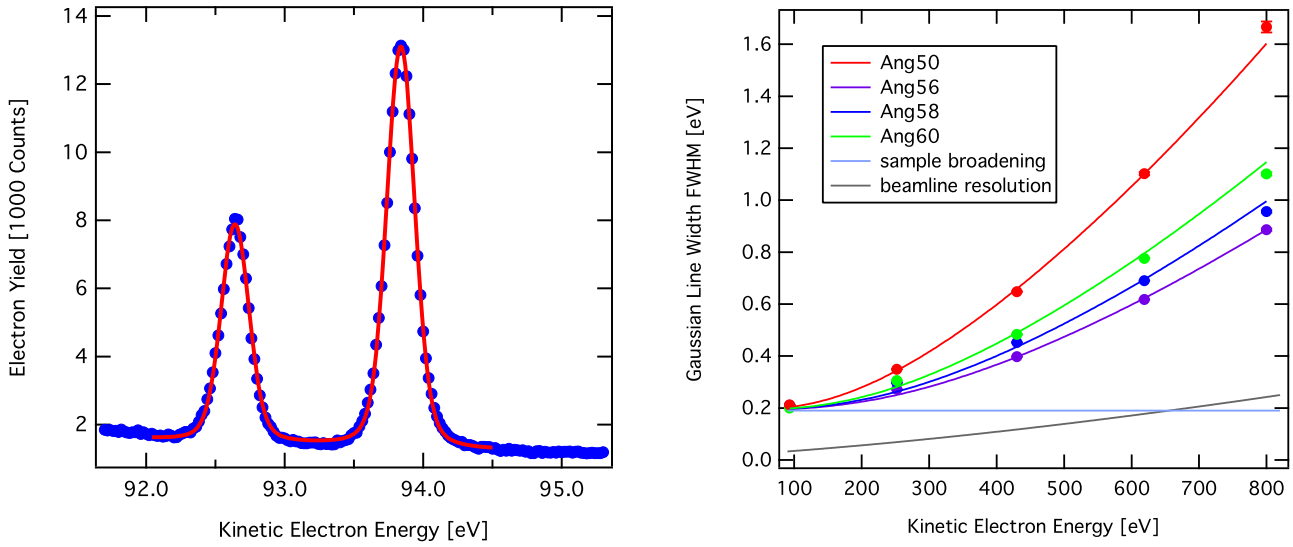

Fig. 4. Left: Angle integrated (±28°) energy spectrum of S2p photoelectrons (blue dots) with E_{ph} =260 eV recorded in the Ang56_4-lens mode. A fit containing 2 Voigt profiles and a linear background (red line) is applied to the data. Right: Gaussian line width contribution in S2p spectra experimentally determined for five different kinetic energies (dots) for different lens modes. The fits to the data account for sample broadening (light blue curve) and beamline resolution (grey curve).

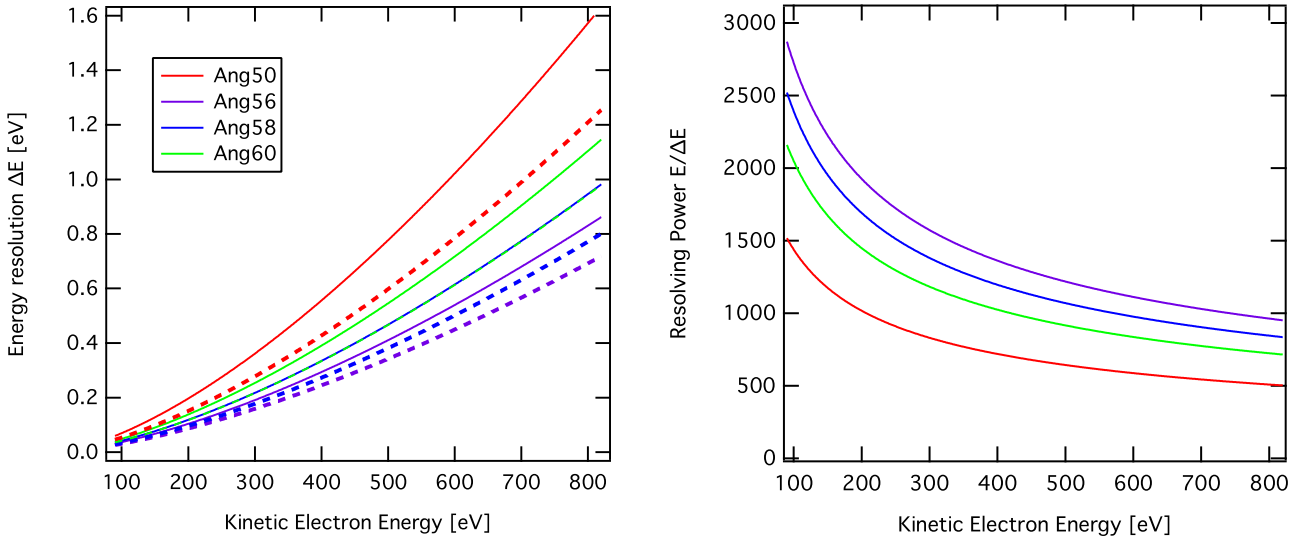

Fig. 5. Left: Global energy resolution (solid lines) calculated with α_{glob} and local energy resolution (dashed lines) calculated with α_{loc} Right: Resolving power of the spectrometer calculated with α_{glob} from the energy resolution fit. Same colour code as in left.

obtained from the photon peak fit tool, for example for Ang56_4-lens mode:

$$\alpha_{matr} \cdot \Delta t_{loc} = 1.76 \cdot 10^{5} \mathrm{eV}^{-0.5} \cdot \mathrm{s}^{-1} \cdot 166\mathrm{ps} =$$
$$2.92 \cdot 10^{-5} \mathrm{eV}^{-0.5} \approx 3.06 \cdot 10^{-5} \mathrm{eV}^{-0.5} = \alpha_{loc} \cdot \Delta t$$

We find that the kinetic energy dependence of the resolution for all four lens modes are in very good agreement with the expected energy resolution in the local case, see Fig. 4. This already shows clearly that the timing system of the spectrometer is working locally as expected. However, it should be emphasized that the fits are made over a wide energy range. Although the fit is in very good agreement with theoretical expectations and point to a resolving power as shown in Fig. 5, the intrinsic sample energy broadening is too high to prove the resolving power at low energies. Further experiments are needed to determine the energy resolution in the UPS regime.

One can further compare the local and the global energy resolution. We find that the global energy resolution is decreased with respect to the local energy resolution by about 20% for all lens modes. Possible reasons are residual misalignments, different signal propagation times of different detector areas and increasing α (fit parameter) at higher emission angle. We are confident that careful alignment and a detector position adapted time correction, which will be available in future, can further improve the global energy resolution.

Apparently the degradation of the global energy resolution is sensitive to the size of the energy window which could be explained by the fact that the electron flight times need to be more compressed for larger energy windows and are therefore more strongly influenced by signal propagation delays between different detector positions.

Comparing the four lens modes one can clearly see the general trend that larger size of the energy window and larger angle acceptance are to the disadvantage of the energy resolution. There-

fore the optimum choice of the lens mode depends on the specific experimental demands.

5. Conclusion

In this work we have operated the 60° wide angle acceptance ARTOF at the femto slicing beamline at BESSY II. Four different lens modes have been investigated in the soft X-Ray regime for kinetic energies of the electrons ranging from 90 eV to 810 eV. All lens modes perform as expected in the full energy range, particularly the resolving power and angle acceptance are in very good agreement with simulations. A high resolving power of 1000 is demonstrated even for high energies and suggests a resolving power of 3000 for 90 eV kinetic energy. Electron spectroscopic techniques, driven by pulsed light sources, that rely on high transmission, high energy resolution, wide angle acceptance or high angular resolution e.g. ARPES, XPD, pump-probe spectroscopy might strongly benefit from the new wide angle lens.

Acknowledgment

Technical support by Mike Sperling is gratefully acknowledged. Pål Palmgren and Patrik Karlsson from Scienta Omicron GmbH are acknowledged for fruitful discussions about the ARTOF.

D.K., F.S, R.J and A.F. acknowledge funding from the ERC-ADG-2014 – Advanced Investigator Grant No. 669531 EDAX under the Horizon 2020 EU Framework Programme for Research and Innovation. NM and SS acknowledge funding from the European Research Council under the European Union's Seventh Framework Programme (FP7/2007-2013)/ERC grant agreement n° [321319], and support from the Carl Tryggers foundation for scientific reseach/CTH), and the Swedish Research Council (VR)

The authors thank HZB for the allocation of beamtime.

References

[1] N. Mårtensson, P. Baltzer, P. Brühwiler, J.-O. Forsell, A. Nilsson, A. Stenborg, B. Wannberg, J. Electron Spectrosc. Relat. Phenom. 70 (no. 2) (1994) 117–128.
[2] B. Wannberg, Nucl. Instrum. Methods Phys. Res., Sect. A 601 (no. 1–2) (2009) 182–194 (Special issue in honour of Prof. Kai Siegbahn.).
[3] G. Öhrwall, P. Karlsson, M. Wirde, M. Lundqvist, P. Andersson, D. Ceolin, B. Wannberg, T. Kachel, H. Dürr, W. Eberhardt, S. Svensson, J. Electron Spectrosc. Relat. Phenom. 183 (no. 1–3) (2011) 125–131 (Electron Spectroscopy Kai Siegbahn Memorial Volume.).
[4] R. Ovsyannikov, P. Karlsson, M. Lundqvist, C. Lupulescu, W. Eberhardt, A. Föhlisch, S. Svensson, N. Mårtensson, Journal of Electron Spectroscopy and Related Phenomena 191 (2013) 92–103.
[5] A. Vollmer, R. Ovsyannikov, M. Gorgoi, S. Krause, M. Oehzelt, A. Lindblad, N. Mårtensson, S. Svensson, P. Karlsson, M. Lundvuist, T. Schmeiler, J. Pflaum, N. Koch, J. Electron Spectrosc. Relat. Phenom. 185 (no. 3–4) (2012) 55–60.
[6] U.B. Cappel, S. Plogmaker, J.A. Terschlusen, T. Leitner, E.M.J. Johansson, T. Edvinsson, A. Sandell, O. Karis, H. Siegbahn, S. Svensson, N. Mårtensson, H. Rensmo, J. Soderstrom, Phys. Chem. Chem. Phys. 18 (2016) 21921–21929.
[7] K. Holldack, R. Ovsyannikov, P. Kuske, R. Müller, A. Schälicke, M. Scheer, M. Gorgoi, D. Kühn, T. Leitner, S. Svensson, N. Mårtensson, A. Föhlisch, Nat. Commun. 5 (2014) 05.
[8] D.F. Förster, B. Lindenau, M. Leyendecker, F. Janssen, C. Winkler, F.O. Schumann, J. Kirschner, K. Holldack, A. Föhlisch, Opt. Lett. 40 (2015) 2265–2268.
[9] C. Strahlman, Time-of-Flight Ion and Electron Spectroscopy: Applications and Challenges at Storage Ring Light Sources Doctoral Thesis, MAX IV Laboratory, Lund University, Sweden, 2016.
[10] K. Holldack, J. Bahrdt, A. Balzer, U. Bovensiepen, M. Brzhezinskaya, A. Erko, A. Eschenlohr, R. Follath, A. Firsov, W. Frentrup, L. Le Guyader, T. Kachel, P. Kuske, R. Mitzner, R. Müller, N. Pontius, T. Quast, I. Radu, J.-S. Schmidt, C. Schüßler-Langeheine, M. Sperling, C. Stamm, C. Trabant, A. Föhlisch, J. Synchrotron Radiat. 21 (2014) 1090–1104.
[11] S. Mattila, J. Leiro, M. Heinonen, T. Laiho, Surf. Sci. 600 (no. 24) (2006) 5168–5175.